RSC Advances

PAPER

View Article Online
View Journal | View Issue

Cite this: *RSC Adv.*, 2026, **16**, 23803

Generic microfluidic platform for digital droplet-based bioassays

Julia Sophie Böke, †[ace] Cornelia Reuter, †*[abc] Mark Kielpinski,[a] Anett Reichert,[ab] Iris Prinz,[d] Daniel Horner,[d] Adrian Prinz,[d] Fritz Bichler,[d] Rudolf Aichinger,[d] Anton Rettenbacher,[d] Georg Bauer,[d] Maria Bauer,[d] Susanne Pahlow,[abc] Karina Weber[a] and Thomas Henkel *[a]

Received 23rd March 2026
Accepted 7th April 2026

DOI: 10.1039/d6ra02395a

rsc.li/rsc-advances

Digital droplet-based bioassays (ddAssays) have been applied in numerous fields, though many existing microfluidic platforms are tailored to specific assay classes and require complex workflows involving multiple processing steps. Here, we present a fully integrated microfluidic platform for generic digital bioassays that combines droplet generation and storage for on-chip incubation and optical readout on a single disposable device. This microfluidic platform enables the parallel execution of test and control experiments, each using more than 200 000 monodisperse droplets of 35 pL. CFD simulations of the step emulsification unit, together with experimental characterization, confirm the predicted device performance. The device is prepared by variothermal compression molding. A dual-layer photoresist strategy was used to create the master for replicating the channel systems with two different channel heights and step transitions between them. The core functionality and the applicability of various optical modalities for image-based readout are demonstrated by exemplary biochemical and microbial growth reporter assays. The platform is compatible with automated image-based analysis for high-throughput digital assay readout.

Introduction

Digital bioassays[1,2] represent an advanced refinement of conventional bioassays, improving sensitivity, precision and throughput.[3] Enumeration of the positive sub-volumes allows absolute quantification of the analytical species present in the original sample. In digital droplet-based bioassays (ddAssays), the target sample is stochastically encapsulated within micro-droplets, which are tested for the absence or presence of the analytical species. These assays often include an amplification step for signal enhancement, *e.g.*, nucleic acid amplification using polymerase chain reaction (PCR) in digital PCR[2,4] or proliferation of cells in the case of digital microbial assays.[5] Most technological advancements focus on specific assay classes, such as PCR,[6,7] enzyme-linked immunoassay (ELISA) or cell-based assays.[7]

Since the breakthrough of encapsulating deoxyribonucleic acid (DNA) in droplets using microfluidics,[8,9] ddPCR platforms have been applied in numerous applications.[10,11] Commercial state-of-the-art devices using ddPCR, as reviewed by Tan *et al.*, are Naica by Stilla Technologies, the QX series and RainDrop, both by Bio-Rad Laboratories.[12] Naica is prefilled with the continuous phase. Summarized, the QX series and Naica have similar capabilities, with around 25 000 droplets of approximately 500 pL partitioned volume per sample, leading to a droplet diameter of approximately 100 μm, and 20 μL total reaction volume. The RainDrop can produce up to 1×10^7 droplets, with a droplet diameter of 17 μm and respective volume of 5 pL, in a total reaction volume of up to 50 μL.[12,13]

The field of digital droplet-based ELISA (ddELISA) is less advanced than ddPCR, as it relies on the isolation of functionalized beads in picoliter droplets for protein quantification.[14,15] Its complexity arises from the challenge of bead encapsulation and the inherently weak fluorescence signal of single-enzyme detection, which lacks PCR-like amplification.[14]

In droplet-based microfluidics,[16] a diluted aqueous sample is partitioned through an often perfluorinated oil phase into droplets.[9,17,18] This approach combines emulsion systems with precise liquid handling in continuous-flow microfluidics. The most common approaches for on-chip droplet generation

[a]*Leibniz Institute of Photonic Technology, Member of the Research Alliance "Leibniz Health Technologies", The Leibniz Centre for Photonics in Infection Research (LPI), Albert-Einstein-Straße 9, 07745 Jena, Germany. E-mail: cornelia.reuter@leibniz-ipht.de; thomas.henkel@leibniz-ipht.de*

[b]*InfectoGnostics Research Campus Jena, Center for Applied Research, Philosophenweg 7, 07743 Jena, Germany*

[c]*Friedrich Schiller University Jena, Institute of Physical Chemistry and Abbe Center of Photonics, Helmholtzweg 4, 07743 Jena, Germany*

[d]*STRATEC Consumables GmbH, Sonystr. 20, 5081 Anif, Salzburg, Austria*

[e]*Cluster of Excellence - Balance of the Microverse, Friedrich Schiller University Jena, 07743 Jena, Germany*

† J. S. B. and C. R. contributed equally.

include step emulsification (SE),[19,20] and flow-focusing[21] on nozzles,[22,23] T-junctions[24,25] or X-junctions.[26,27]

Kaminski *et al.* summarized the progression of droplet microfluidics, focusing on its relevance to microbiology. Ongoing developments aim to improve droplet stability and generation rates. Methods have been developed to support the growth of microorganisms with dissolved gases such as oxygen and CO_2.[6] Various microfluidic platforms exist and have been used to implement ddAssays at different levels of integration. Microchannels with prolonged residence time[28] have been used for decades to enable flow-through incubation, *e.g.*, in combination with thermocyclers for PCR.[29] Schuler *et al.* developed a centrifugal microfluidic platform that combines droplet generation and PCR amplification within a single device architecture,[30] while Schulz *et al.* presented a highly integrated digital PCR system that enables sample-to-answer nucleic acid detection using step emulsification and on-chip thermocycling.[31] In parallel, several studies have focused on improving droplet generation throughput and monodispersity. Xu *et al.* parallelized 2000 nozzles for spontaneous droplet generation of pL-volume governed by a Laplace pressure difference at the SE unit.[23] Wei *et al.* designed a microfluidic chip that employs step emulsification to directly generate droplets into the storage reservoir, producing droplets with diameters of 38.2 μm and 110.3 μm.[13] Comparable work by Zhang *et al.* achieved high-throughput droplet formation using 50 parallel step emulsification units, generating uniform ~175 μm droplets with a coefficient of variation (CV) of 3% at flow rates of 1.4–17.5 nL s^{-1}.[32] Lastly, the application of deep learning algorithms has shown promise in further lowering detection limits for rapid classification and analysis.[33]

Despite significant progress in droplet microfluidics, many existing systems are tailored to specific assay types, rely on complex workflows involving multiple devices or off-chip transfer steps between droplet generation, incubation, and readout, use unconventional microfluidic device footprints or require specialized instrumentation for their operation. This limits their flexibility and increases the risk of droplet loss or instability during handling. In addition, popular commercial platforms require prefilled microfluidic devices or specialized preparation procedures, which complicate operation and reduce compatibility with standard laboratory workflows.

In this work, we present a generic microfluidic platform for ddAssays that integrates droplet generation, incubation, storage, and optical readout on a single disposable microfluidic chip. The platform supports two assay units, each with more than 200 000 droplets, implemented on the footprint of a standard microscopy slide, enabling direct image-based readout with conventional microscopy systems. The droplets remain in the storage unit during the assay[34] but can be released and completely recovered if needed. Initial filling with custom fluids and reagents can be easily done on-site as a part of the assay workflow. The droplet generator design is guided by rational design principles and validated by computational fluid dynamics (CFD) simulations[35–38] and experimental characterization. The device is prepared by STRATEC Consumables GmbH using variothermal injection-compression molding, a technology established for high-volume replication of microstructured polymer components. In this paper, we demonstrate the operation of the microfluidic ddAssay chip in terms of initial filling with the continuous phase, sample droplet formation, incubation and on-chip readout. Application examples across digital droplet-based assay classes are presented and discussed, and compatibility with various optical readout modalities is demonstrated.

Results and discussion

Microfluidic concept and implementation

The microfluidic device aims to implement all essential microfluidic operation units required for digital droplet-based bioassays (ddAssays), including droplet generation and storage for incubation, and optical readout, within a single integrated microfluidic platform. DdAssays follow a very simple and generic workflow. After sample preparation, the sample volume is partitioned into droplets for incubation and readout. During readout, the number of positive and negative droplets is counted and used to derive the analytical result. The integrated microfluidic device is designed to support the steps of droplet generation, prolonged storage and incubation, image-based readout, and collection of the droplets into an external vial. Following the rules of the microfluidic platform concept[39] the system is composed of interoperable microfluidic operation units as shown in Fig. 1. In our work, compatibility of the units is achieved by a design process where each unit is drafted by rational design and verified by *in silico* testing using modern CFD approaches, as exemplarily reported in the paper for the droplet generator unit, following the rules of microfluidic design automation.[26,40] The clear advantage of this approach is

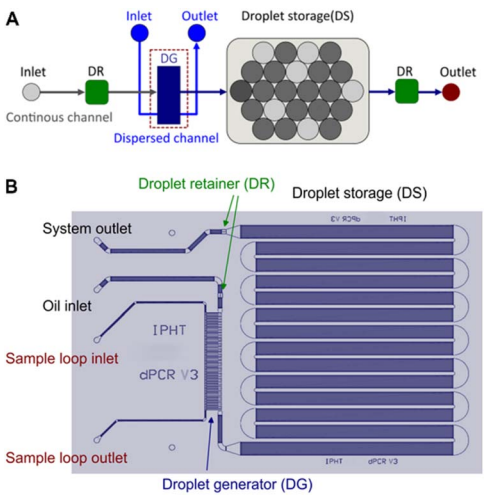

Fig. 1 Microfluidic platform diagram of the ddAssay chip, represented by (A) a sequence of interconnected microfluidic operation units. SL_{in}: sample loop inlet, SL_{out}: sample loop outlet, oil_{in}: continuous phase inlet, DR: droplet retainer, DG: droplet generator, DS: droplet storage, incubation and readout channel. (B) Arrangement of microfluidic operation units for layout. It is mirrored for the complete microfluidic device.

that the fully functioning devices were obtained from the first preparation run.

Sample loop unit (SL)

The on-chip sample loop channel delivers the sample liquid from an inlet port to the feed channels of the droplet generator unit. It additionally connects to an outlet port to completely exchange the contained liquid when loading a sample or to vent the channel. It measures 30.8 mm in length, 0.16 mm in width, and 0.04 mm in depth, with an internal volume of 197 nL.

Droplet generator unit (DG)

The droplet generator unit operates according to the principle of step emulsification (SE).[20,41] This is realized by an abrupt transition in channel height from a shallow to a deep channel section, whereby the dispersed-phase sample fluid is passed through the shallow feed channel and overflows into the deep channel, which is filled with the continuous-phase fluid. Droplet generation happens at the transition from a shallow to a deep channel as the dispersed-phase fluid droplet grows into the deep channel. The process itself is dominated by interface-generated forces. Shear flow of the continuous phase is not required, reducing the required fraction of continuous-phase fluid. This enables the direct creation of densely packed droplet suspensions.[42] Parallelization enables scalable droplet generation rates.[23,32,43] In digital microfluidics, direct contact between the dispersed phase fluid and the channel walls is prevented by the formulation of the continuous phase fluid in combination with the wetting properties of the channel surface. All channel surfaces are designed to exhibit ideal non-wetting conditions for the dispersed aqueous phase. Under these conditions, the effective contact angle approaches 180°, preventing wetting of the channel walls by the dispersed phase and minimizing droplet adhesion or crosstalk between droplets *via* wall-sticking droplet fragments. Details have been previously investigated by the authors.[44,45] Its implementation for CFD simulation has been reviewed by Hoang *et al.*[36]

The unique selling point of the designed droplet generator is that droplet volume and generation rate can be easily predicted by simple geometrical rules. In the rational design phase, the geometric and control parameters are adjusted to the defined process parameters using mathematical models. Afterwards, it is validated by *in silico* experiments using CFD simulations. Therefore, this structure can be easily customized and integrated into microfluidic networks.

Design model

The designed droplet generator comprises 92 step emulsification units, with their inlets connected to the sample loop and their outlets to the droplet-collecting channel. Each step emulsification unit consists of a neck section and a trapezoidal-shaped head section that ends at the channel step, where droplet detachment occurs (Fig. 2). The neck channel serves as a throttle, limiting the flow rate through the droplet generator structure to ensure controlled interface break-up during droplet formation. It has a square cross-section of 12 × 12 μm^2. The

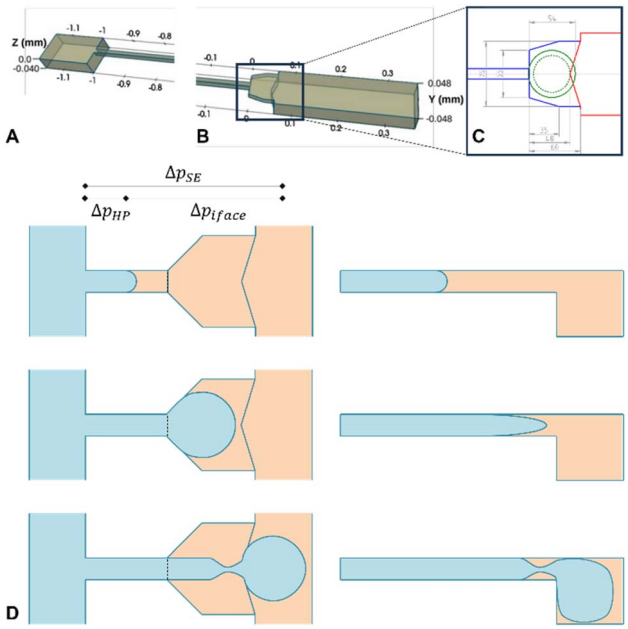

Fig. 2 Droplet generator (DG) composed of (A) a neck and (B) a head section. (C) Technical sketch of the DG head section with the droplet shape fitted into the model. Green line: droplet circumferential shape, green dotted: contact line of the droplet with the bottom face, blue: vertical side walls of the SE unit, red: vertical side walls of the step and the droplet collecting channel. (D) Process of droplet generation. Blue: dispersed phase fluid, orange: continuous phase fluid.

neck channel length must be determined within the framework of the rational design. The head section has a trapezoidal shape with a height of 12 μm and vertical side walls. It is connected to the neck channel and the droplet collecting channel, which has a height of 40 μm. The head section must be dimensioned to collect a dispersed-phase volume before it is discharged over the step into the droplet collecting channel.

For the released droplet, a diameter of 38 μm ($V = 28.7$ pL) was specified in advance. Around 200 000 droplets should be generated in less than two minutes, which requires a droplet generation rate in the order of >1500–2000 droplets per second and a total flow rate of >50 nL s^{-1} for the dispersed phase fluid.

Rational design – head section

To achieve the target droplet volume of 28.7 pL, a slightly smaller volume of the dispersed phase must be accumulated in the head section before release. This is necessary, since the flow into the droplet continues until the formed droplet is completely released from the unit. After droplet release, a fraction of the volume remains in the unit. Therefore, a smaller design volume of 25 pL is used in the rational design to define the geometrical parameters for the head section.

Within the head section, the accumulated liquid forms a disk-shaped body with half-circular side walls before being released into the droplet-collecting channel. The volume of this body can be calculated from its height H and diameter D using eqn (1), obtained by integrating the droplet shape in cylindrical coordinates.

$$V = \frac{5\pi H^3}{12} - \frac{\pi^2 H^3}{8} - \frac{\pi D H^2}{2} + \frac{\pi^2 D H^2}{8} + \frac{\pi D^2 H}{4} \quad (1)$$

For a design volume of 25 pL and a height of 12 μm, the diameter evaluates to 54 μm at the center plane of the body. The head section can be constructed by fitting this body into the geometry in Fig. 2C.

Rational design – neck length

During operation, the unit is filled with the aqueous phase except for a small part of the head section (Fig. 2D). Therefore, the viscosity of water is used in the following calculations. Viscous losses in the head section were neglected due to its short length. For predicting the volume flow through the step emulsification unit, the viscous losses along the neck channel, and the back pressure p created by the curved liquid–liquid interface inside the head section need to be considered according to eqn (2).

$$p_{\text{SE unit}} = p_{\text{HP}} + p_{\text{iface}} \quad (2)$$

Pressure drop due to viscous losses is predicted using the Hagen–Poiseuille model with the hydraulic diameter approximation for channels with non-circular cross-section. The model eqn (3) already includes the simplifications for square channel cross-sections. The symbol μ represents the viscosity, L the length, Q the volume flow and H the width and height of the channel. The negative sign reflects the pressure drop $p = p_{\text{out}} - p_{\text{in}}$.

$$p_{\text{HP}} = -\frac{128\mu L Q}{\pi H^4} \quad (3)$$

To predict the interface-generated back pressure, the Laplace equation is used, where σ denotes the interface tension and R_1 and R_2 the vertical and horizontal radii of curvature of the liquid–liquid interface. The negative sign reflects the orientation of the curved interface relative to the channel direction from inlet to outlet.

$$p_{\text{iface}} = -\left(\frac{\sigma}{R_1} + \frac{\sigma}{R_2}\right) \quad (4)$$

The merged models provide the pressure/throughput characteristics for either p or Q as the independent parameters.

$$p_{\text{SE unit}} = -\frac{\sigma}{R_1} - \frac{\sigma}{R_2} - \frac{128\mu L Q}{\pi H^4} \quad (5)$$

$$Q_{\text{SE unit}} = -\frac{\pi\sigma H^4}{128\mu L R_2} - \frac{\pi\sigma H^4}{128\mu L R_1} - \frac{\pi H^4 p}{128\mu L} \quad (6)$$

The target system with parallelized step emulsification units is operated at a constant pressure drop between the sample loop and droplet collecting channel as discussed before. Onward, the specified pressure reflects the pressure settings, so that the minus sign disappears unless it is explicitly stated that it is the negative pressure drop. During droplet generation, the curvature of the liquid–liquid interface in the head section periodically changes, resulting in fluctuations in the flow rate.

These volume flow fluctuations are illustrated in Fig. 3 for the volume flow dependent on the diameter of the growing droplet disk in the head section. At low pressure settings of 10 mbar, the interface-generated back pressure is not compensated, and negative volume flow towards the inlet is observed. For pressure settings >20 mbar, volume flow is permanently directed to the outlet.

During droplet release, the volume accumulated in the head section is spilled into the droplet-collecting channel as a spherical droplet with a lower pressure drop across the interface compared to the disk-shaped volume part inside the head section. This causes the liquid to be expelled from the head section into the droplet. At the end of this process, the droplet is released by interface rupture. This requires that the volume flow through the unit be limited. For reliable operation, we expect that the volume flow ratio q_{ratio} through the SE unit at the time of droplet release (Fig. 2F) should be less than 1.25 times the volume flow when filling the head section (Fig. 2E). This value is defined in eqn (7) where R_1 represents the radius of the vertical, R_2 the radius of the horizontal curvature of the maximum volume body inside the neck section and R_3 represents the radius of the droplet immediately before interface rupture.

$$q_{\text{ratio}} = \frac{Q_{\text{SE unit}}(p,\ R_3,\ R_3, \ldots)}{Q_{\text{SE unit}}(p,\ R_1,\ R_2, \ldots)} \quad (7)$$

Substitution and simplification yield eqn (8),

$$q_{\text{ratio}} = \frac{(R_2 + R_1)R_3\sigma + R_1 R_2 R_3 p}{2R_1 R_2\sigma + R_1 R_2 R_3 p} \quad (8)$$

where the value of q_{ratio} depends on the particular curvatures of the interfaces, the interface tension and the pressure drop p along the complete SE unit. It should be mentioned that q_{ratio} is

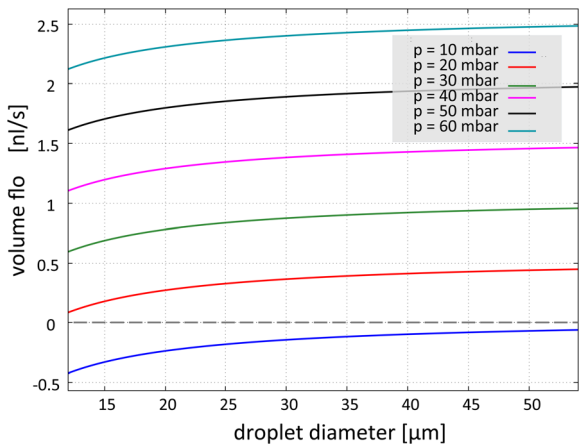

Fig. 3 Volume flow fluctuations through a single SE unit depending on the diameter of the growing droplet disc inside the head section for a dynamic viscosity of 10^{-3} Pa s and an interface tension of 5×10^{-3} N m^{-1} and a neck channel length of 1 mm.

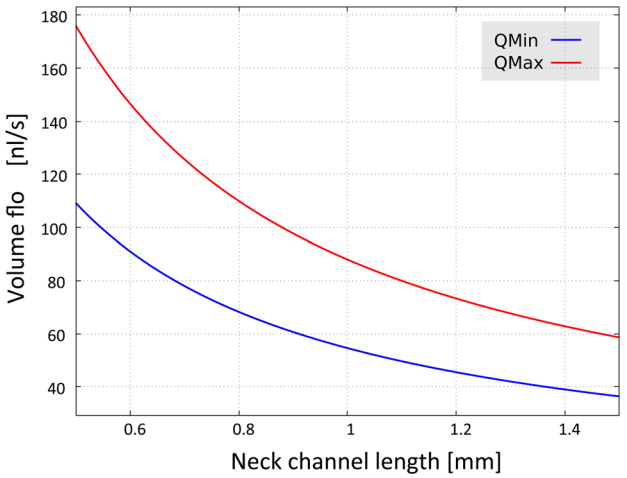

Fig. 4 Minimum and maximum volume flow through the parallelized droplet generator with 92 SE unit elements dependent on the neck channel length.

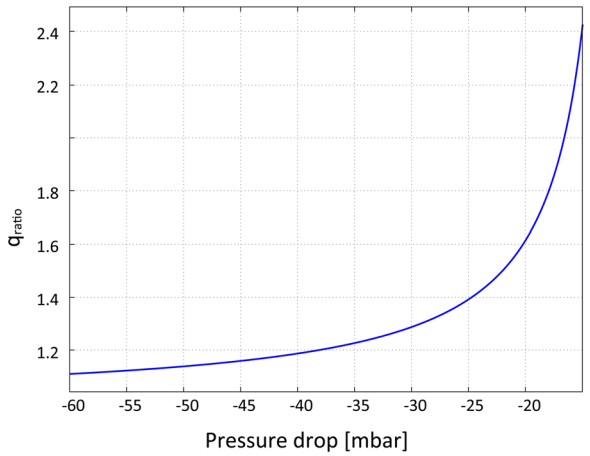

Fig. 5 Volume flow ratio q_{ratio} parameter dependent on the pressure drop over the SE unit for an interface tension of 5 mN m^{-1} and the target design parameters $R_1 = 6$ µm, $R_2 = 27$ µm and $R_3 = 17$ µm. Negative pressure drop corresponds with a positive pressure settings value.

not influenced by the length L of the neck channel since it has been eliminated from the equation during simplification.

The pressure dependency of the q_{ratio} parameter is shown in Fig. 5 for the target-step emulsification unit. The value of $q_{ratio} < 1.25$, where the unit is expected to work in a reliable regime, is found at a pressure setting of 3000 Pa (30 mbar).

Now, the length of the neck channel is defined so that the volume flow at 3000 Pa matches the desired volume flow to achieve the desired droplet generation rate.

The maximum and minimum volume flow for the parallelized droplet generator with 92 SE unit elements, as a function of the neck channel length, are shown in Fig. 4. A volume flow of 80 nL s^{-1} can be achieved with a neck channel length of 1 mm.

Table 1 CFD simulation parameters

Transport properties		
Fluid[a]	HFE 7200	Water
Density	1610 kg m^{-3}	997 kg m^{-3}
Dynamic viscosity	0.770 10^{-3} Pa s	0.890 10^{-3} Pa s
Interface tension	5.5 × 10^{-3} N m^{-1}	
Interface property (fluid/wall)		
Contact angle	0°	180°
Boundary conditions (fluid/wall)		
Outlet pressure	fixedValue 0 Pa	Uniform 0 Pa
Inlet pressure	fixedValue 0 Pa	Uniform 3000.0 Pa

[a] At 25 °C.

CFD simulations

The droplet generator geometry was validated by CFD simulations‡ to analyze droplet formation dynamics. Accordingly, the geometry shown in Fig. 2A was investigated.

Simulations of the droplet generation process were performed using the interFoam solver of the OpenFoam CFD toolkit,[35,36] version 2406. Post-processing and visualization were performed using ParaView,[37] based on VTK.[38] A zero-contact-angle boundary condition was applied by setting the contact angle between the continuous phase fluid and channel wall to 0°.[46] Details are provided in the Materials and methods section. The template case for rerunning the simulation is provided in the digital supplement.

In the simulation, a pure pressure-driven flow was used, with fixed pressure constraints at the inlet and outlet faces, and a pressure drop of 3000 Pa between them. This corresponds to a single-step emulsification unit within the parallelized droplet generator, in which all 92 units were fed from a single sampling channel at (almost) identical pressure. Fluid properties and simulation parameters are summarized in Table 1. The throughput through the unit depends on the steepness of the pressure gradient, which is influenced by the Laplace pressure drop across the evolving interface of the formed droplets, as discussed in the Rational design – head section.

As long as the interface is within the neck channel section, where it has the smallest curvature, as shown in Fig. 6B, the minimum flow rate is observed. The situation reflects the initiation process, in which the continuous oil phase in the neck channel is successively substituted by the sample fluid.

The droplet generation cycle starts when the interface expands into the head section and forms a disc-shaped body. As shown in Fig. 6C and D, the horizontal radius of curvature increases, thereby reducing the pressure drop across the interface. Due to the fixed pressure settings at the inlet and outlet, the pressure drop along the neck channel increases, thereby

‡ Provided in the digital supplement S1.

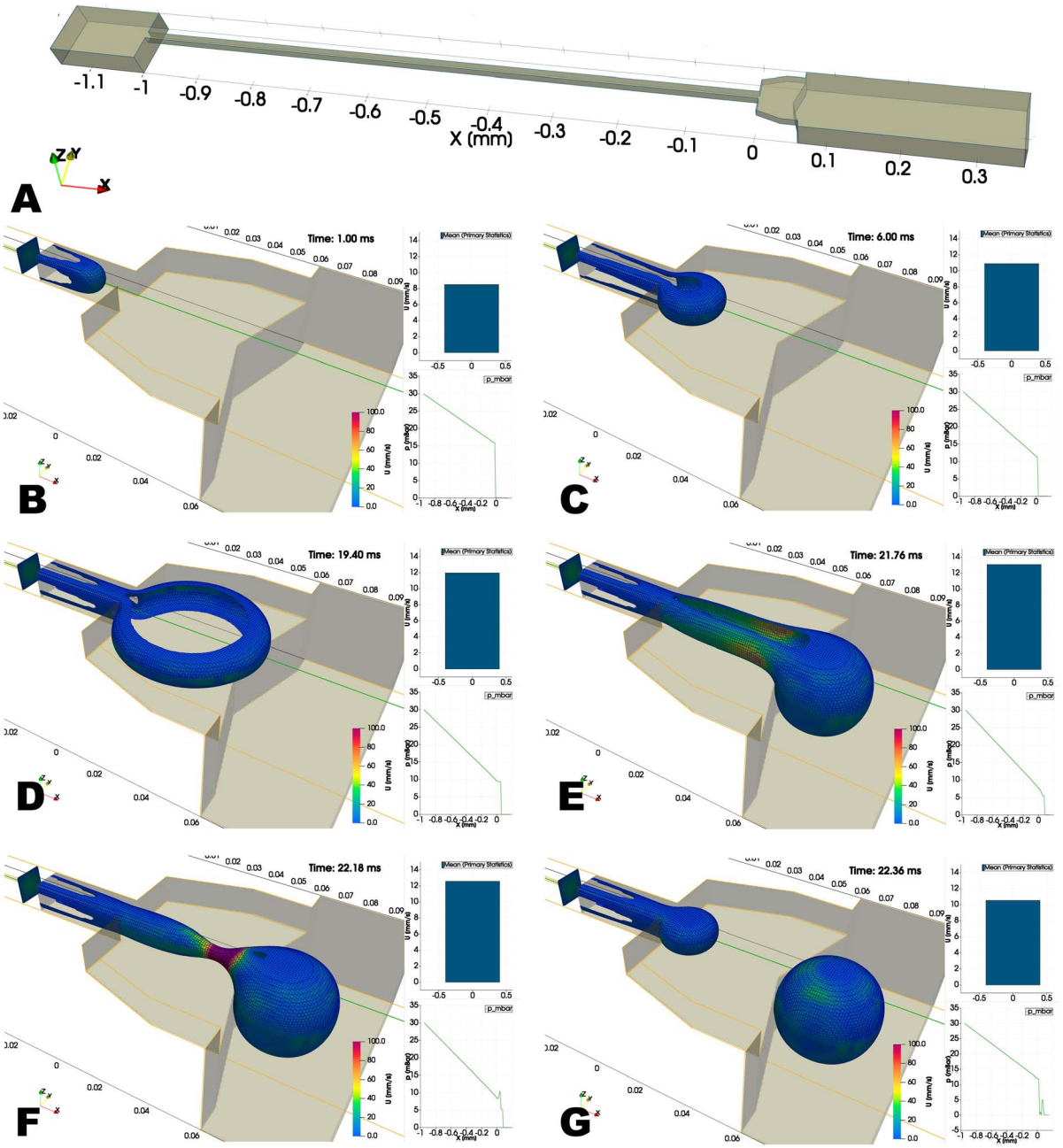

Fig. 6 Visualization of CFD results‡ with fixed inlet pressure – constraint. (A) Domain overview for the single droplet generator unit showing the sample loop channel, the neck section and the head section with the step transition into the main channel (from left to right). (B–G) Geometry of the liquid–liquid interface at different time steps of the droplet generation cycle. Local interface velocity is visualized by the color map. The mean fluid velocity in the neck channel is shown in the bar chart, and the pressure drop along the *x*-axis (green line) is shown in the line chart insert of each subplot.

increasing the transport velocity of the fluid. The situation reflects the stage at which the liquid forming the droplet accumulates in the head section.

As soon as the interface passes the step in front of the head section, a spherical droplet starts growing into the droplet-collecting channel. Due to the smaller pressure drop across the droplet-shaped interface compared to the disc-shaped interface inside the head section, the liquid accumulated there spills into the growing droplet as visible in Fig. 6C–E. Due to the reduced interface-generated back pressure, the volume flow through the neck channel is also increasing. However, since this is limited by the throttling effect of the neck channel, the phase boundary within the neck section is narrowed, and the droplet formed in the droplet collecting channel breaks off as visible in Fig. 6F. After separation at the interface, the remaining volume in the head section snaps back and the formed droplet is released into the droplet collecting channel.

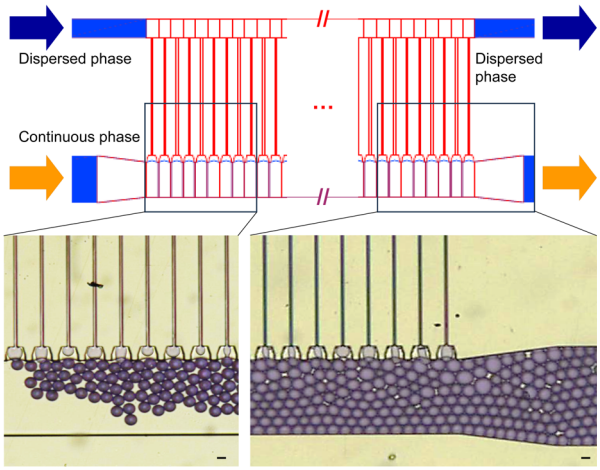

Fig. 7 System sketch and video microscopy snapshot of the parallelized droplet generator, operated at 150 nL s^{-1} sample inflow rate. Only the leftmost and rightmost part of the droplet generator are shown. Droplets leave the droplet generator as a densely packed emulsion. Scale bar: 20 μm.

Now that the droplet generation cycle is completed, the next cycle starts.

In the simulations, the droplet generation cycle takes 16.8 ms, corresponding to a droplet generation rate of 60 Hz. For the parallelized droplet generator with 92 droplet generator units, the simulations predict a total droplet generation rate of ~4550 droplets per second and a sample volume flow rate of 140 nL s^{-1}, which is sufficient to fill the chip with droplets in less than 1 minute.

Experimental confirmation

The final geometry of the droplet generator unit has been implemented by arranging the investigated droplet generator structures in parallel (Fig. 7). It operates efficiently at a high sample-to-continuous phase ratio, enabling the direct generation of densely packed droplet suspensions. This approach eliminates the need to remove a surplus of the continuous phase before loading the suspension into the storage and incubation chamber.

This experimentally confirms the generation of a densely packed droplet suspension with a droplet volume of 35 pL at a total sample flow rate of 150 nL s^{-1} and a droplet generation rate of around 4300 droplets per second. CFD results and experimental data are in good agreement.

Minor variations in droplet diameter can occur during formation but remain sufficiently small for digital assay applications. Additionally, each droplet volume can be determined by image-based readout, allowing accurate quantification.

In summary, the droplet generator is confirmed to produce droplets of suitable size and droplet generation rate. The confirmed droplet generation rate and sample flow rate are three times higher than the initially drafted parameters and can be scaled down to a sample flow rate of 50 nL s^{-1} for the experiments.

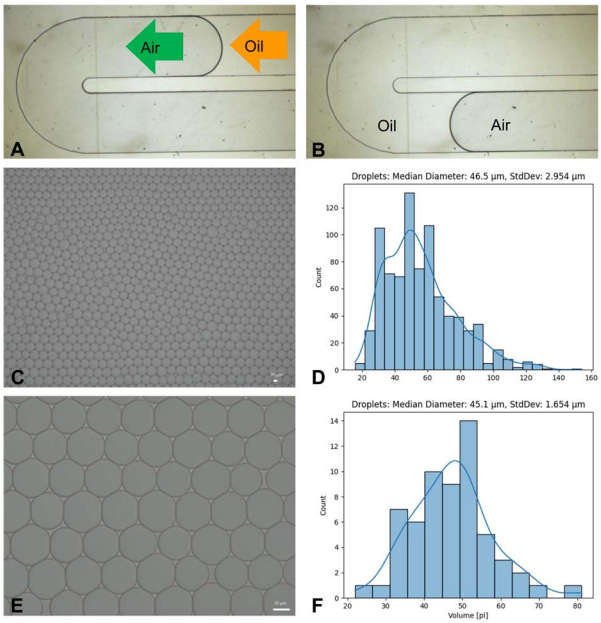

Fig. 8 Initial filling with the continuous phase (A and B). Exemplary overview of droplets in the storage chamber (C and E) with their respective histogram for the droplet diameter distribution (D and F). Scale bar: 20 μm.

Droplet storage unit (DS)

The droplet storage is implemented as a winding capillary slit channel (Fig. 1) having a width of 1.2 mm, a mean channel length of 272.8 mm, a height of 40 μm and an inner volume of 13.1 μL. Initial filling of the chip device with the continuous phase is performed at 50 nL s^{-1}, where a convex liquid–air interface forms and is continuously transported through the channel. Droplet suspensions can be loaded into the initially filled channel (Fig. 8).

Considering hexagonal dense packaging, it can hold up to 252 000 droplets with a diameter of 40 μm. In the case of cubic dense packaging, the number of droplets reduces to 204 000. If the optically measured droplet diameter falls below the channel height of 40 μm, the sphere volume equation can be used. Otherwise, the volume V_{RB} of a rotational body with flat top and bottom face, as given in eqn (1), is recommended.

Droplet retainer unit (DR)

The main purpose of the droplet retainer unit is to prevent droplets from escaping from the storage unit during incubation and readout. In addition, it supports air-bubble-free initial filling of the chip with the continuous-phase fluid and the option to transfer the stored droplets completely to an external reservoir for further post-processing. The challenge of meeting all these contradictory requirements was solved by a special shape of a droplet retention barrier, for which a patent[34] was granted.

The droplet retainer unit is realized as a biconcave plateau structure with a center duct spanning the width of the main channel, with a plateau height of 28 μm, and a minimum duct

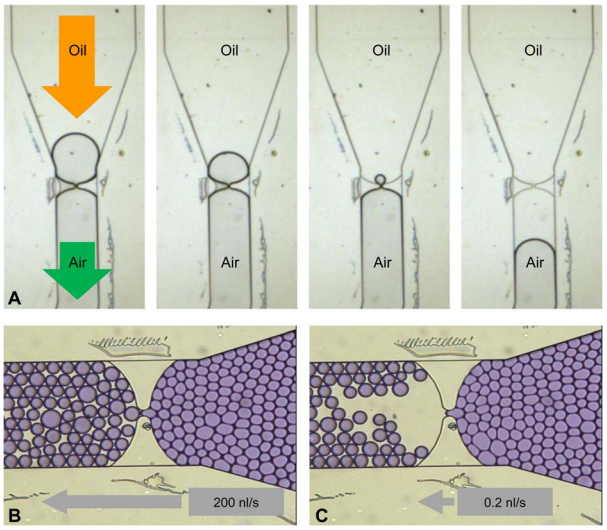

Fig. 9 (A) Residue-free transportation of air bubbles facilitated by the retainer structure. (B) Passage of droplets through the retainer structure at high flow rates. (C) Retention of small droplets and confinement of the assay in the storage unit through the retainer structure.

width of 18 μm. The main channel height is 40 μm, and the main channel width is 1200 μm. Such a plateau can be passed by the continuous-phase fluid. At low flow rates, any droplet or air bubble will be retained, which corresponds to the target functionality. In certain scenarios, however, the droplets must also pass the barrier in a defined way. This applies when sample droplets need to be collected into an external reservoir, or when large air bubbles have to pass through the barrier during initial filling without leaving any air fragments behind. Both situations can be managed. Depending on the applied flow rate, droplet size and interface tension, droplets can pass through the duct or overcome the barrier across the full width of the main channel.

All targeted functionalities are experimentally confirmed and shown in Fig. 9A. A flow rate of 50 nL s^{-1} is used for the continuous phase fluid HFE7500 containing 2% of the surfactant dSurf. The air bubble passes through the barrier duct without fragmentation. Droplets with a diameter between 30 and 40 μm can be retained for droplet storage during incubation and readout at continuous-phase flow rates below 0.2 nL s^{-1} (Fig. 9C), which is below the parasitic flow rates induced by thermal or inertial effects during incubation. This flow rate can also be used to supply the growing cultures with gases dissolved in the continuous phase liquid. In this case, the complete liquid exchange can be achieved within 4.5 h.

Optionally, the chip can be detached from the fluid management system, and the fluid ports can be sealed with adhesive tape without disturbing the arrangement of the stored droplets. The droplet retainer contributes to this operation by retaining the droplets inside the storage and incubation unit. This makes the fluid management available for other tasks, *e.g.*, next ddAssay platform filling, and improves the optical accessibility of the chip for optical readout using microscope objectives.

Integrated microfluidic device – from layout to fabrication

The microfluidic operation units are connected (Fig. 1) and laid out on the footprint of a microscopy slide to realize the integrated microfluidic device for droplet-based assays and control measurement. For the realization of the two etching depths, 12 μm and 40 μm, a dual-layer resist strategy is realized through injection compression molding, which achieves a surface flatness/roughness in the order of 1 μm mm^{-2}.

Injection compression molding technology[47] was originally developed for the mass production of optical data storage media such as CDs, DVDs, and Blu-ray discs, which require the precise replication of sub-micron surface relief structures. The process employs interchangeable master plates carrying the surface microstructures, allowing rapid adaptation of the mold insert. The molding cycle comprises injection, compression, and demolding steps. During injection, the polymer melt is introduced into the mold at a temperature above its melting point and subsequently cooled to a temperature between the melting and softening points. In the compression step, the polymer is pressed against the master plate to accurately replicate the surface microstructures and to define the final thickness of the workpiece. After demolding, the replicated disc is available for post-processing and finishing.

For the fabrication of microfluidic devices, the channel geometries must be implemented on the master plate as surface-relief structures with a small draft angle to enable reliable demolding. The realization of channel sections with different heights on a single substrate requires master plates featuring multiple structure depths, which significantly complicates master fabrication. During post-processing, fluidic access holes are introduced, the microchannels are sealed by bonding to a cover layer, and the individual chips are subsequently separated from the molded disc.

The presented microfluidic device was prepared from the cyclic olefin polymers, COP1420R (molded part) and COC6013M (cover film). A dual-layer photoresist strategy, based on sequential lithographic processing, is used to generate channel geometries and microfluidic operation units, followed by an electroplating process to convert them into a nickel master plate.

Achieving accurate alignment between the two layers, controlling the photoresist thicknesses, and incorporating an appropriate draft angle (typically < 2°) are critical process considerations to ensure successful demolding in subsequent manufacturing steps.

This dual-layer resist strategy enables the precise generation and reliable replication of the required geometries.[48] High replication accuracy and excellent dimensional agreement with the design were achieved even for the challenging geometries of the parallelized droplet generator (Fig. 10) and the droplet retainer structures.

The variothermal molding process significantly enhances replication quality by suppressing premature solidification and uncontrolled polymer relaxation during cooling, which is critical for preserving fine microstructural features with high

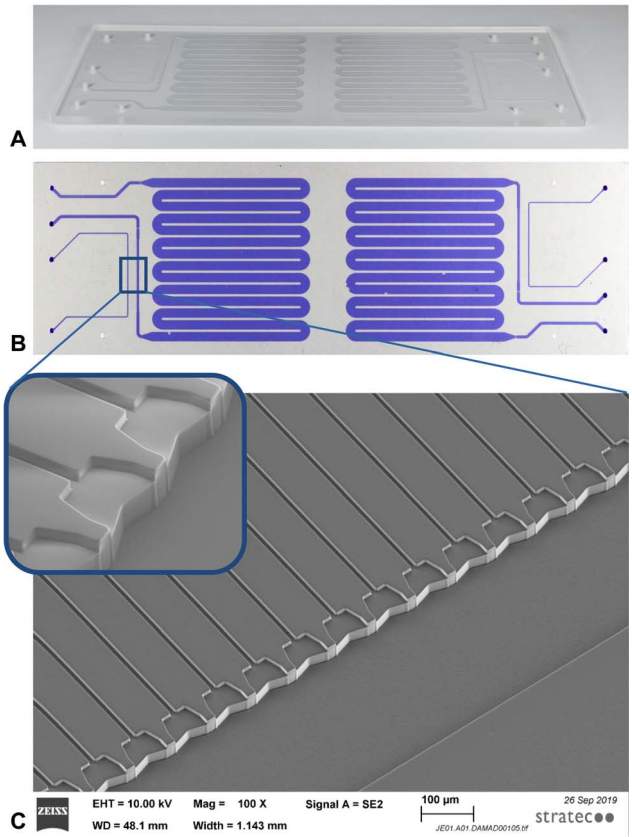

Fig. 10 (A) Image of the fabricated microfluidic platform and (B) channels filled with blue dye for enhanced contrast. (C) SEM picture with zoom-in of nozzles, head section, and a step into the droplet-collecting channel created in COP1320R.

aspect ratios and for minimizing defects such as weld lines, flow marks, and sink marks.

About 1000 devices have been prepared with uniform quality within multiple batches. Batch-to-batch variability is influenced by several factors, including material batch variations, material pretreatment, and, most critically, the condition and quality of the mold stamper. While the variothermal process primarily improves the molding and demolding of fine microstructures, careful control of material properties and stamper integrity was maintained to minimize inter-batch variability.

Digital droplet-based assay application scenarios

Exemplary digital helicase-dependent amplification for DNA detection. A digital nucleic acid amplification assay was conducted as a representative use case to validate the functionality of the developed device and verify the accuracy of its fluid and sample management protocols. Advancements in nucleic acid-based identification methods are crucial for improving rapid diagnostics in sepsis, particularly for pathogens like *Acinetobacter baumannii* (*A. baumannii*), which are increasingly recognized as significant contributors to pneumonia.[49]

A digital helicase-dependent amplification (HDA)[50,51] assay was performed for the quantification of *A. baumannii* DSM30007 DNA. Droplets were created from a total volume of a nucleic acid amplification reaction mixture of 15 µL, which was loaded into the interconnection tubing of the sample syringe and attached to the short tubing at the chip mount using polydimethylsiloxane (PDMS) sleeves.

A second syringe filled with Novec HFE7500 was attached in the same way to the mineral oil inlet tubing of the chip mount. The outlet capillary of the sampling was opened. At this point, the initial filling procedure is started at a flow rate of 50 nL s^{-1} until the oil phase reaches the outlet capillary of the sampling loop.

This procedure takes about 3–4 minutes, depending on the length of the interconnecting capillary. Continuous-phase fluid flow continues during the subsequent operations until the droplet generation and loading process is finished. Subsequently, the sampling fluid is forwarded at a flow rate of 50 nL s^{-1} into the sampling loop until the preceding air has been completely passed through the sampling loop and the sample fluid has reached the open end of the capillary. The sample flow is stopped, and the sampling loop outlet is sealed by sticking a pin needle into the capillary. Following that, the system is ready to generate and load the droplets into the store. Droplets are generated at a flow rate of 150 nL s^{-1} for the sample fluid and 50 nL s^{-1} for the continuous oil phase. Under these conditions, the droplet generation and loading procedure is completed after 62 seconds, when the first droplets arrive and pass the outlet droplet retainer structure of the chip, and a total sample volume of 9.34 µL is converted into droplets. Fluid connections can be detached, the capillaries are closed with needles, and the device is incubated at 65 °C for one hour to complete the HDA. The droplet arrangements are subsequently read out using fluorescence microscopy (Fig. 11A and B).

Droplet dense packaging is preserved during the amplification and incubation procedure. Fluorescent positive droplets

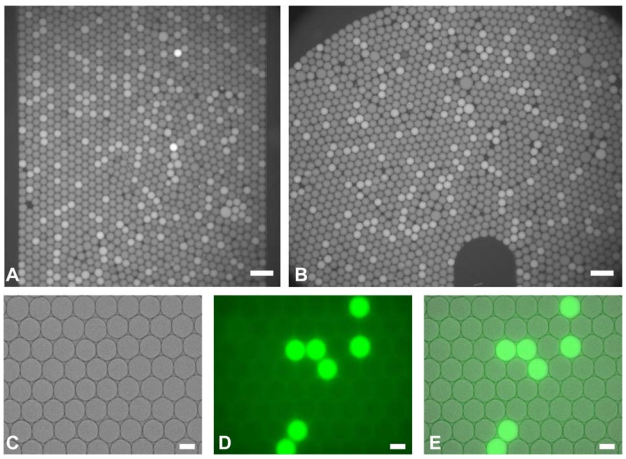

Fig. 11 Fluorescence image-based on-chip read-out of the digital HDA assay for (A) a straight section of the droplet storage and for (B) a reverse loop of the same. Scale bar: 100 µm. Brightfield and fluorescence image-based on-chip readout of the digital microbial assay for *E. coli* Nissle 1917 after 20 h of incubation in the storage chamber. (C) Brightfield images and (D) fluorescence images observed with 40× objective, fluorescence and brightfield (E) image overlay. Scale bar: 20 µm.

and non-fluorescent negative droplets are clearly discriminated and can be applied to the subsequent data analysis for counting the number of positive and negative droplets.[52]

Exemplary application of droplet-based microbial growth assay. As another application scenario for the integrated, generic microfluidic system, we demonstrate single-cell microbial assays using *Escherichia coli* Nissle 1917 (EcoN)[53] with the potential to address current clinical applications.

Droplets were generated from an initial bacterial suspension (300 μL), which was loaded into the interconnection tubing of the sample syringe and connected to the short tubing at the chip mount utilizing PDMS sleeves. The flow rates are adjusted to ensure stable droplet formation. During droplet generation, the bacterial suspension and the continuous phase are supplied at flow rates of 150 nL s^{-1} and 50 nL s^{-1}, respectively. The droplets are collected in the droplet storage, and the chip is transferred to an incubator set at 37 °C for 6–20 hours to allow proliferation. After incubation, the droplets are analyzed using fluorescence microscopy to assess cell viability and growth. The readout of one representative microfluidic chip, as well as the associated imaging overlay, is presented in Fig. 11C–E. Successful growth of *E. coli* Nissle 1917 within the droplets was observed after the incubation period, as evidenced by a progressive increase in cell density and corresponding fluorescence signal. Brightfield imaging confirms the presence and proliferation of bacterial colonies, while fluorescence imaging reveals distinct signal development, indicating active expression of the fluorescent dye. The uniformity of growth across droplets demonstrated consistent encapsulation and stable culture conditions within the microfluidic system. Fluorescent-positive droplets and non-fluorescent-negative droplets are clearly distinguished and can be applied to the subsequent data analysis. The droplets remained stable throughout the experiment and maintained large size uniformity, without droplet merging observed over 24 hours, ensuring consistent microenvironments for bacterial cultivation.

Materials and methods

CFD simulations

CFD-simulation, postprocessing and rendering of results have been processed on a PC Prime H370-PLUS (ASUSTek Computer Inc., Germany) with an Intel® Core™ i5-9600KF CPU and 16 GB RAM running the Debian GNU Linux 12 (bookworm) operating system using the interFoam solver of the OpenFoam CFD toolkit,[35,36] version 2406. Postprocessing and rendering of the simulation results have been performed with the ParaView data analysis and visualization toolkit.[37]

The full case template for running the simulation is provided in the digital supplement under the file name <stepEmuV3ScaledFixedInletPressureTemplate>. Dimensions and parameters have been scaled to the base units of 1.0 mm for length, 1.0 s for time, and 1.0 mg for mass to ensure numerical stability in the CFD simulations. All parameters and fluid properties are given in the ParametersAndScaling spreadsheet table in the ParametersAndScaling subfolder of the case template. A hexagonal volume mesh has been generated from a surface triangulated mesh of the SE unit using the snappyHexmesh utility with a uniform cell size in x, y, z of 0.86, 0.86, 0.86 μm^3.

The outlet patch was set to the 'inletOutlet' type for velocity, fixedValue' type with $p = 0$ Pa for pressure and 'inletOutlet' type for the phase fraction alpha.water.

The inlet patch was set to the 'pressureInletOutletVelocity' type for velocity, 'fixedValue' type with $p = 3000$ Pa for pressure and 'inletOutlet' type for the phase fraction alpha.water.

Channel walls have been set to 'notSlip' type for velocity, fixedFluxPressure' type for pressure and 'constantAlphaContactAngle' with theta0 = 180.0°.

The fluid properties of water and Novec HFE7500, with an interfacial tension of 5.5×10^{-3} N m^{-1}, have been used for both the continuous and dispersed phases.

Dynamic time-step sizing was activated, with the Courant number limited to maxCo = 0.05. The neck channel was initially filled with the dispersed-phase fluid using the setFields utility of the OpenFoam Toolkit.

The shape of the liquid/liquid interface was initially allowed to converge using manual control and increasing the time step size, starting with delta$T = 1 \times 10$ s. The simulation was allowed to run for 23 ms, which was sufficient to model the creation and release of a single droplet.

Finally, the simulation results were converted to the generic, long-term-supported VTK data format using the toolkit's 'foamToVTK' utility and saved in the 'VTK_RESULTS' subfolder. All parts of the simulation can be controlled by starting the related run script.

Details are provided in the Readme.txt file in the root folder of the case template. For rerunning the postprocessing with ParaView, the respective pvsm state files from the VTK_RESULTS_ALL or VTK_RESULTS_SUBSET folder can be loaded into the ParaView app, where the VTK_RESULTS_SUBSETS folder contains all the data for reproducing Fig. 6.

Microfluidic device manufacturing and operation

Two-step photolithography. The microfluidic consumable is fabricated using injection-compression molding, based on a two-layer UV-LIGA-fabricated master structure. The realization of the two-layer master structure was accomplished through sequential lithographic processing. Fig. 12 illustrates the stepwise fabrication procedure.

Initially, a 12 μm-thick first lithographic layer of the negative photoresist SU-8 3010 was spin-coated, soft-baked, exposed, and post-baked (Fig. 12A), but not developed. Following the post-exposure bake, a second photoresist layer with a thickness of 29 μm was spin-coated on top of the first layer and subsequently exposed with an alignment accuracy of approximately 2 μm relative to the initial pattern (Fig. 12B and C). After exposure, a development step using PGMEA solvent was carried out to selectively remove the unexposed regions of both resist layers, thereby generating a dual-level lithographic structure (Fig. 12D).

To produce the injection-molding insert, the two-level lithographic master was replicated in a nickel mold *via*

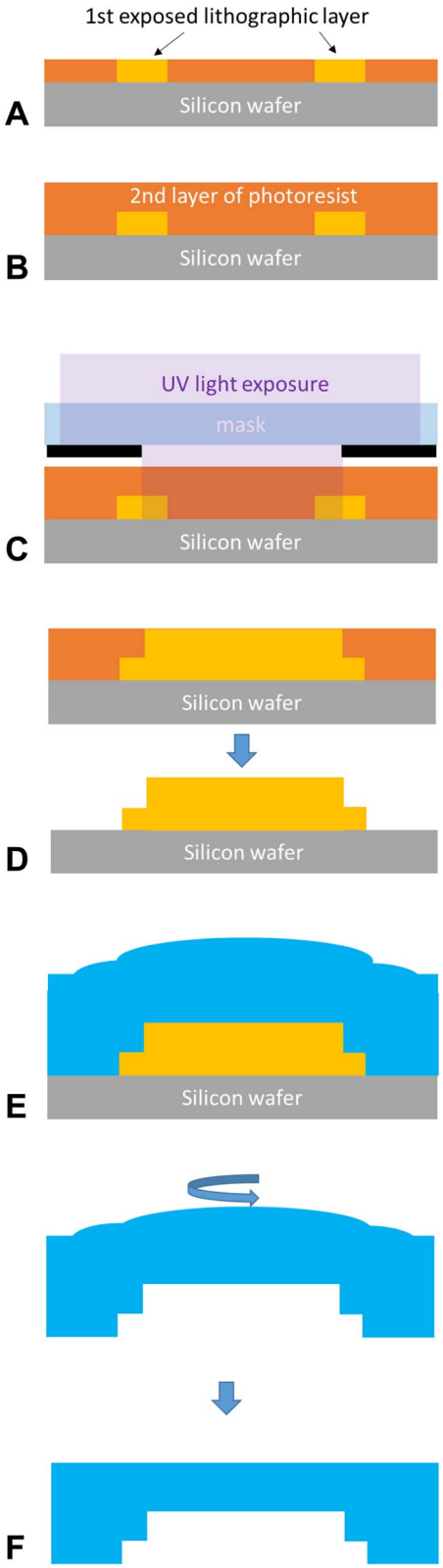

Fig. 12 Schematic illustration of the process steps involved in two-level lithographic insert manufacturing: (A) exposure of the first lithographic layer, (B) spin coating of the second photoresist layer, (C) masked UV exposure of the second layer, (D) development of the exposed regions, (E) nickel plating of the developed pattern, (F) polishing and shaping of the insert for subsequent molding.

electroplating of around 300 μm thickness (Fig. 12E). After nickel deposition, the backside of the mold insert was polished to achieve a flat surface while preserving the integrity of the microstructures. The final polished nickel insert then served as the mold insert for the injection molding process (Fig. 12F).

Molding. For molding, a former Blu-ray disc manufacturing process was adapted to generate injection-molded parts with a thickness of 1.2 mm made in COP1420R. In order to replicate the structures successfully, a variothermal[48] compression molding process is applied. Prinz *et al.* reported the details on the injection molding process.[48]

Postprocessing and packaging. In order to manufacture the final ddAssay device, the microstructured cycloolefin copolymer slide (COP1420R) is bonded to a cyclic olefin copolymer cover film (COC6013M), with a thickness of 180 μm, by a solvent-assisted thermal bonding technique, established within STRATEC Consumables as a standard process for high-volume manufacturing of microfluidic devices.

The four fluid ports on each side are drilled with a diameter of 0.6 mm. They are arranged with a line spacing of 3 mm, a hole spacing of 4.5 mm, and an offset of 2.25 mm.

Solvent-assisted thermal bonding is a proprietary internal process of STRATEC Consumables GmbH. It is a technique that does not require additional materials like adhesive layers. The principle works like this: the COP is activated by a solvent on the surface, and both parts are bonded by decent heat and pressure (typical ranges for such bonding are 60–90 °C) in a custom-specific bonding setup. Due to the activation, only the upper surface becomes soft, making it possible to bond channels with very high precision. Global flatness <100 μm could be achieved after bonding, without leakage or crosstalk of channels. A channel height precision with a tolerance of around 1 μm was achieved.

Fluid interconnection block. A special fluidic connector (Fig. 13) provides a tight, death-volume-free connection between the microfluidic chip and the tubing. The elimination of HPLC fitting screws offers a grid of 9 ports accommodated in a field measuring 23 × 9 mm.

The fluidic connector consists of three main parts: the upper part with through holes for the tubing/screws and a mold for a rubber seal. The lower counterpart generates the clamp force.

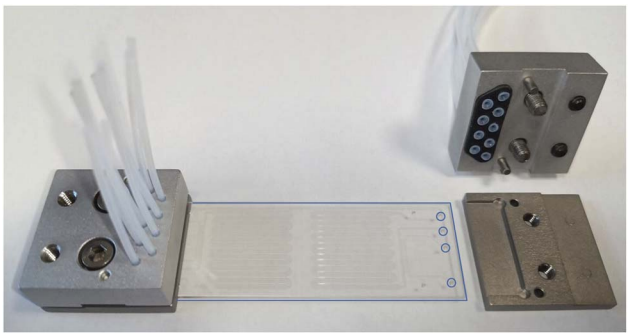

Fig. 13 The fluid interconnecting block on the left side connects PTFE tubings to the chip. The block on the right shows the inner compartments and sealings with flanged tubings and positioning pins.

Additionally, screws and pins are inserted to clamp the assembly and to adjust the parallel alignment of the upper and lower parts.

The mounting is guided by a recess for inserting the chip and two pins. Sealing is achieved by deforming the seal as the connector closes, generating a seal-to-chip and seal-to-tubing contact.

The PTFE tubings, size OD 1.59 mm/ID 0.5 mm (BOLA, Bohlender GmbH, Grünsfeld, Germany), were flanged with the easy-flange tool (VICI Jour, Schenkon, Switzerland). The rubber seal is made by compression molding of HYPEX HX61 MB (TKV Thermoform GmbH, Pößneck, Germany). The upper part is made of aluminum, whereas the lower part is made of stainless steel.

Brightfield and fluorescence microscopy. For process monitoring and characterization of microfluidic devices by video microscopy, a 12× zoom lens system (Navitar Inc., Rochester, NY, USA) has been used in combination with a digital camera aca1920-40μm (Basler AG, Ahrensburg, Germany) and a 3000 K white light source MWWHLP2 (Thorlabs GmbH, Bergkirchen, Germany), mounted to an XT95 vertical optical rail (Thorlabs GmbH, Bergkirchen, Germany).

Brightfield and fluorescence images for assay data acquisition are obtained using either a 10×/NA 0.5 objective (Zeiss, Oberkochen, Germany) or 10×/NA 0.45 and 40×/NA 0.95 objectives (KEYENCE Deutschland GmbH, Neu-Isenburg, Germany).

Fluid management. For fluid management, the high-precision syringe pumps NeMeSys (Cetoni GmbH, Korbuβen, Germany) were used in combination with precision syringes (Innovative Labour System (ILS), Ilmenau, Germany).

For the continuous phase fluid, Novec HFE7500 (3M, St. Paul, Minnesota, USA) has been used in combination with the surfactant dSurf (Fluigent, Le Kremlin-Bicêtre, France) at a working concentration of 2% (w/v).

Helicase-dependent amplification assay. An HDA assay was performed using a commercially available helicase-dependent amplification kit, IsoAMPIII universal tHDA (New England Biolabs, Ipswich, MA, USA), containing a 25× reaction buffer with $MgCl_2$, dNTPs, DNA helicase, strand-displacing DNA polymerase, and enzyme mix. Purified genomic DNA was used as the template and combined with forward and reverse primers (final concentration 0.15 μM each) in a total reaction volume of 25 μL. For fluorescence-based detection, an intercalating fluorescent dye EvaGreen (Biotium, Fremont, CA, USA) was added according to the manufacturer's instructions, and nuclease-free water was used to adjust the final volume. Reactions were assembled in 0.2 mL PCR tubes, gently mixed, and briefly centrifuged before droplet generation.

Microbial growth assay. Samples (1 mL) from starter cultures of *Escherichia coli* Nissle 1917 (EcoN) obtained by overnight growth in LB medium (Merck KGaA, Darmstadt, Germany) with shaking (120 rpm) were centrifuged for 5 min at 7700 rpm and resuspended in fresh potassium morpholinopropane sulfonate (MOPS) minimal medium (Carl Roth GmbH + Co. KG, Karlsruhe, Germany) supplemented with 0.2% glucose. Subsequently, the optical density (OD) was measured at 600 nm using a visible spectrophotometer (Eppendorf SE, Hamburg, Germany). Cell suspensions were diluted in fresh minimal medium to cell concentrations of 10^8, 10^6, 10^4, and 10^2 CFU mL^{-1} to obtain a sufficient droplet occupancy. For fluorescence-based experiments in droplets, 0.1 μM CalceinAM as a viability dye was added. Diluted bacterial suspensions were transferred to 1.5 mL Eppendorf tubes before droplet generation.

Conclusions

The presented platform provides a flexible microfluidic architecture for implementing different classes of ddAssays within a single integrated device. The microfluidic chip integrates the complete set of necessary microfluidic operation units. The microfluidic device consists of 92 parallelized step emulsification units, enabling fast, homogeneous droplet generation and on-chip droplet storage for incubation and optical readout. Our microfluidic platform reliably retains droplets within the storage unit throughout the experiments, while controlled release and recovery remain possible when required.

First, the rational design of the droplet generator is confirmed by *in silico* evaluation *via* CFD simulations. The droplet generator is designed to hold a droplet volume of 25 pL, resulting in an experimentally confirmed droplet volume of 35 pL at a total sample flow rate of 150 nL s^{-1} and a droplet generation rate of around 4300 droplets per second. Considering hexagonal dense packing, the ddAssay can hold up to 252 000 droplets with a diameter of 40 μm and can be filled in less than two minutes. Thus, rational design, CFD simulations and experimental data demonstrate good agreement.

Second, the microfluidic device is fabricated as a single-use device according to the design parameters by injection-compression molding, using a two-layer resist strategy for master preparation. Two independent assay structures for the parallel execution of test and control experiments are realized on the footprint of a standard microscope slide. Approximately 1000 microfluidic devices were produced with uniform quality across multiple batches, highlighting the quality and robustness of the fabrication process and the well-thought-out design of the microfluidic platform.

As the final proof, we demonstrate two bioassays that highlight the versatility of the presented generic digital droplet-based bioassay platform. A digital helicase-dependent amplification (HDA) assay for *Acinetobacter baumannii* DSM30007 DNA confirms reliable droplet generation, storage, incubation, and fluorescence-based readout, validating the platform for digital nucleic acid amplification assays. In addition, a droplet-based single-cell growth assay using *Escherichia coli* Nissle 1917 enables monitoring of bacterial viability and growth dynamics at the single-droplet level, demonstrating the platform's capability for quantitative microbiological assays and its potential applicability in microbiome research.

The high droplet throughput of the presented platform further motivates the use of artificial intelligence-based image analysis for automated process control, multiplex droplet identification, and scalable downstream data processing in future digital bioassay applications.

Author contributions

Conceptualization: C. R., I. P., K. W., T. H.; data curation: T. H.; formal analysis: J. S. B., T. H.; funding acquisition: K. W.; investigation: J. S. B., C. R., M. K., A. R., I. P., D. H., A. P., F. B., R. A., A. Rb., S. P., T. H.; methodology: C. R., A. R., I. P., K. W., T. H.; project administration: D. H., G. B., M. B., K. W.; resources: G. B., M. B., S. P., K. W.; software: T. H.; supervision: I. P., K. W., T. H.; validation: J. S. B., C. R., M. K., A. P., F. B., T. H.; visualization: J. S. B., C. R., M. K., I. P., T. H; writing – original draft: J. S. B., C. R., M. K., I. P., T. H.; writing – review & editing: J. S. B., C. R., M. K., T. H.

Conflicts of interest

There are no conflicts to declare.

Data availability

Additional data is stored in accordance with the Leibniz Association and DFG guidelines at Leibniz-IPHT and will be made available upon request.

The data supporting this article have been included as part of the supplementary information (SI). Supplementary information: CFD template case in S1 and videos supporting the experimental details S2. See DOI: https://doi.org/10.1039/d6ra02395a.

Acknowledgements

This work is supported by the BMFTR, funding program Photonics Research Germany (FKZ: 13N15704) and is integrated into the Leibniz Center for Photonics in Infection Research (LPI). The LPI initiated by Leibniz-IPHT, Leibniz-HKI, UKJ and FSU Jena is part of the BMFTR national roadmap for research infrastructures. We also acknowledge the funding by the German Federal Ministry of Research, Technology and Space, Germany (BMFTR) grant EXASENS (13N13856). The authors thank Lydia Lehniger for preliminary studies. AI-assisted technologies (such as Large Language Models) were used for writing assistance.

References

1 A. S. Basu, Digital Assays Part I: Partitioning Statistics and Digital PCR, *SLAS Technol.*, 2017, **22**, 369–386.
2 B. Vogelstein and K. W. Kinzler, Digital PCR, *Proc. Natl. Acad. Sci. U. S. A.*, 1999, **96**, 9236–9241.
3 Y. Zhang and H. Noji, Digital Bioassays: Theory, Applications, and Perspectives, *Anal. Chem.*, 2017, **89**, 92–101.
4 C. Reuter, S. Hentschel, A. Breitenstein, E. Heinrich, O. Aehlig, T. Henkel, A. Csáki and W. Fritzsche, Chip-based duplex real-time PCR for water quality monitoring concerning Legionella pneumophila and Legionella spp, *Water Environ. J.*, 2021, **35**, 371–380.
5 H. Ma, Y. Zhang, R. Shen and Y. Jia, Droplet-Based Microfluidics in Single-Bacterium Analysis: Advancements in Cultivation, Detection, and Application, *Biosensors*, 2025, **15**(8), 535.
6 T. S. Kaminski, O. Scheler and P. Garstecki, Droplet microfluidics for microbiology: techniques, applications and challenges, *Lab Chip*, 2016, **16**, 2168–2187.
7 A. S. Basu, Digital Assays Part II: Digital Protein and Cell Assays, *SLAS Technol.*, 2017, **22**, 387–405.
8 I. Schneegass and J. M. Köhler, Flow-through polymerase chain reactions in chip thermocyclers, *J. Biotechnol.*, 2001, **82**, 101–121.
9 B. J. Hindson, K. D. Ness, D. A. Masquelier, P. Belgrader, N. J. Heredia, A. J. Makarewicz, I. J. Bright, M. Y. Lucero, A. L. Hiddessen, T. C. Legler, T. K. Kitano, M. R. Hodel, J. F. Petersen, P. W. Wyatt, E. R. Steenblock, P. H. Shah, L. J. Bousse, C. B. Troup, J. C. Mellen, D. K. Wittmann, N. G. Erndt, T. H. Cauley, R. T. Koehler, A. P. So, S. Dube, K. A. Rose, L. Montesclaros, S. Wang, D. P. Stumbo, S. P. Hodges, S. Romine, F. P. Milanovich, H. E. White, J. F. Regan, G. A. Karlin-Neumann, C. M. Hindson, S. Saxonov and B. W. Colston, High-throughput droplet digital PCR system for absolute quantitation of DNA copy number, *Anal. Chem.*, 2011, **83**, 8604–8610.
10 S. Olmedillas-López, R. Olivera-Salazar, M. García-Arranz and D. García-Olmo, Current and Emerging Applications of Droplet Digital PCR in Oncology: An Updated Review, *Mol. Diagn. Ther.*, 2022, **26**, 61–87.
11 Y. Hou, S. Chen, Y. Zheng, X. Zheng and J.-M. Lin, Droplet-based digital PCR (ddPCR) and its applications, *TrAC, Trends Anal. Chem.*, 2023, **158**, 116897.
12 L. L. Tan, N. Loganathan, S. Agarwalla, C. Yang, W. Yuan, J. Zeng, R. Wu, W. Wang and S. Duraiswamy, Current commercial dPCR platforms: technology and market review, *Crit. Rev. Biotechnol.*, 2023, **43**, 433–464.
13 C. Wei, W. Lv, Y. Ding, C. Wang, C. Sun, X. Feng, T. Zhang, J. Li, Q. Li and S. Li, Investigation of co-flow step emulsification (CFSE) microfluidic device and its applications in digital polymerase chain reaction (ddPCR), *J. Colloid Interface Sci.*, 2025, **678**, 1132–1142.
14 J. Yi, Z. Gao, Q. Guo, Y. Wu, T. Sun, Y. Wang, H. Zhou, H. Gu, J. Zhao and H. Xu, Multiplexed digital ELISA in picoliter droplets based on enzyme signal amplification block and precisely decoding strategy: A universal and practical biodetection platform, *Sens. Actuators, B*, 2022, **369**, 132214.
15 L. Cohen, N. Cui, Y. Cai, P. M. Garden, X. Li, D. A. Weitz and D. R. Walt, Single Molecule Protein Detection with Attomolar Sensitivity Using Droplet Digital Enzyme-Linked Immunosorbent Assay, *ACS Nano*, 2020, **14**, 9491–9501.
16 L. Nan, H. Zhang, D. A. Weitz and H. C. Shum, Development and future of droplet microfluidics, *Lab Chip*, 2024, **24**, 1135–1153.
17 J.-C. Baret, Surfactants in droplet-based microfluidics, *Lab Chip*, 2012, **12**, 422–433.
18 A. Reichert, D. Kraus, T. Heckmann, K. Weber and T. Henkel, Application Note - Analysis of a commercial surfactant for digital PCR, https://www.fluigent.com/wp-

content/uploads/2022/01/application_note_dsurf-1.pdf, accessed 25 November 2025.
19 S. Sugiura, M. Nakajima, S. Iwamoto and M. Seki, Interfacial Tension Driven Monodispersed Droplet Formation from Microfabricated Channel Array, *Langmuir*, 2001, **17**, 5562–5566.
20 V. Chokkalingam, S. Herminghaus and R. Seemann, Self-synchronizing pairwise production of monodisperse droplets by microfluidic step emulsification, *Appl. Phys. Lett.*, 2008, **93**, 254101.
21 T. Henkel, T. Bermig, M. Kielpinski, A. Grodrian, J. Metze and J. Köhler, Chip modules for generation and manipulation of fluid segments for micro serial flow processes, *Chem. Eng. J.*, 2004, **101**, 439–445.
22 S. L. Anna, N. Bontoux and H. A. Stone, Formation of dispersions using "flow focusing" in microchannels, *Appl. Phys. Lett.*, 2003, **82**, 364–366.
23 X. Xu, H. Yuan, R. Song, M. Yu, H. Y. Chung, Y. Hou, Y. Shang, H. Zhou and S. Yao, High aspect ratio induced spontaneous generation of monodisperse picolitre droplets for digital PCR, *Biomicrofluidics*, 2018, **12**, 14103.
24 T. Thorsen, R. W. Roberts, F. H. Arnold and S. R. Quake, Dynamic pattern formation in a vesicle-generating microfluidic device, *Phys. Rev. Lett.*, 2001, **86**, 4163–4166.
25 K. Martin, T. Henkel, V. Baier, A. Grodrian, T. Schön, M. Roth, J. Michael Köhler and J. Metze, Generation of larger numbers of separated microbial populations by cultivation in segmented-flow microdevices, *Lab Chip*, 2003, **3**, 202–207.
26 J. S. Böke, D. Kraus and T. Henkel, Microfluidic Network Simulations Enable On-Demand Prediction of Control Parameters for Operating Lab-on-a-Chip-Devices, *Processes*, 2021, **9**, 1320.
27 X. Zhang, S. Wang, J. Wang, X. Sun, J. Xue, Z. Wang, T. Yang, L. Weng, B. Wang and G. Luo, A ddPCR platform based on a microfluidic chip with a dual-function flow-focusing structure for sample-to-result DNA quantification analysis, *Lab Chip*, 2024, **24**, 738–750.
28 L. Frenz, K. Blank, E. Brouzes and A. D. Griffiths, Reliable microfluidic on-chip incubation of droplets in delay-lines, *Lab Chip*, 2009, **9**, 1344–1348.
29 I. Schneegass, R. Brautigam and J. M. Kohler, Miniaturized flow-through PCR with different template types in a silicon chip thermocycler, *Lab Chip*, 2001, **1**, 42–49.
30 F. Schuler, M. Trotter, M. Geltman, F. Schwemmer, S. Wadle, E. Domínguez-Garrido, M. López, C. Cervera-Acedo, P. Santibáñez, F. von Stetten, R. Zengerle and N. Paust, Digital droplet PCR on disk, *Lab Chip*, 2016, **16**, 208–216.
31 M. Schulz, S. Calabrese, F. Hausladen, H. Wurm, D. Drossart, K. Stock, A. M. Sobieraj, F. Eichenseher, M. J. Loessner, M. Schmelcher, A. Gerhardts, U. Goetz, M. Handel, A. Serr, G. Haecker, J. Li, M. Specht, P. Koch, M. Meyer, P. Tepper, R. Rother, M. Jehle, S. Wadle, R. Zengerle, F. von Stetten, N. Paust and N. Borst, Point-of-care testing system for digital single cell detection of MRSA directly from nasal swabs, *Lab Chip*, 2020, **20**, 2549–2561.
32 M. Zhang, J. Li, S. Liang, Y. Li and H. Chen, Designable microfluidic ladder network with gradually varying resistance for mass production of monodisperse droplets, *Microfluid. Nanofluid.*, 2025, **29**(9), 60.
33 Y. Song, S. Lim, Y. T. Kim, Y. M. Park, A. Da Jo, N. H. Bae, S. J. Lee, B. G. Choi, S. G. Im, H. U. Kim and K. G. Lee, Deep learning enables accurate analysis of images generated from droplet-based digital polymerase chain reaction (dPCR), *Sens. Actuators, B*, 2023, **379**, 133241.
34 T. Heckmann, T. Henkel, E. Herbst, G. Mayer, A. Reichert and K. Weber, Mikrotropfenrückhalteanordnung, DPMA Patent Grant DE102019108155B3, 2020.
35 H. Jasak, OpenFOAM: Open source CFD in research and industry, *Int. J. Nav. Archit. Ocean Eng.*, 2009, **1**, 89–94.
36 D. A. Hoang, V. van Steijn, L. M. Portela, M. T. Kreutzer and C. R. Kleijn, Benchmark numerical simulations of segmented two-phase flows in microchannels using the Volume of Fluid method, *Comput. Fluid*, 2013, **86**, 28–36.
37 J. Ahrens, B. Gevici and C. Law, in *Visualization Handbook*, Elsevier, 2005, pp. 717–731.
38 W. J. Schroeder, *The Visualization Toolkit. An Object-Oriented Approach to 3D Graphics ; visualize Data in 3D - Medical, Engineering or Scientific ; Build Your Own Applications with C++, Tcl, Java or Python ; Includes Source Code for VTK (Supports UNIX, Windows and Mac)*, Kitware Inc, Clifton Park, NY, 4th edn, 2006.
39 D. Mark, S. Haeberle, G. Roth, F. von Stetten and R. Zengerle, Microfluidic lab-on-a-chip platforms: requirements, characteristics and applications, *Chem. Soc. Rev.*, 2010, **39**, 1153–1182.
40 N. Gleichmann, D. Malsch, P. Horbert and T. Henkel, Toward microfluidic design automation: a new system simulation toolkit for the *in silico* evaluation of droplet-based lab-on-a-chip systems, *Microfluid. Nanofluid.*, 2015, **18**, 1095–1105.
41 J. Bibette, Depletion interactions and fractionated crystallization for polydisperse emulsion purification, *J. Colloid Interface Sci.*, 1991, **147**, 474–478.
42 C. Priest, S. Herminghaus and R. Seemann, Generation of monodisperse gel emulsions in a microfluidic device, *Appl. Phys. Lett.*, 2006, **88**, 024106.
43 C. Zheng, S. Masui, Y. Kanno and T. Nisisako, Microfluidic Step Emulsification with Parallel Nozzles on a Vertical Slit, *Ind. Eng. Chem. Res.*, 2024, **63**, 10226–10233.
44 D. Malsch, N. Gleichmann, M. Kielpinski, G. Mayer and T. Henkel, in *ASME 2008 6th International Conference on Nanochannels, Microchannels, and Minichannels*, ASMEDC, 2008, pp. 1571–1578.
45 D. Malsch, M. Kielpinski, N. Gleichmann, G. Mayer and T. Henkel, Reconstructing the 3D shapes of droplets in glass microchannels with application to Bretherton's problem, *Exp. Fluid*, 2014, **55**, 1841.
46 D. A. Hoang, V. van Steijn, L. M. Portela, M. T. Kreutzer and C. R. Kleijn, in *AIP Conference Proceedings*, 2012, pp. 86–89.
47 M. Heckele and W. K. Schomburg, Review on micro molding of thermoplastic polymers, *J. Manuf. Syst.*, 2004, **14**, R1–R14.

48 I. Prinz, M. J. Haslinger, M. Mühlberger, G. Reiter, A. Prinz, M. M. Schmidt, T. Schaller, M. Bauer, M. Musso and G. Bauer, Industrial view of plasmonic devices made by nanoimprint or injection molding, *J. Appl. Phys.*, 2021, **129**, 130902.

49 C. Ayoub Moubareck and D. Hammoudi Halat, Insights into Acinetobacter baumannii: A Review of Microbiological, Virulence, and Resistance Traits in a Threatening Nosocomial Pathogen, *Antibiotics*, 2020, **9**, 119.

50 L. Schwenkbier, S. Pollok, S. König, M. Urban, S. Werres, D. Cialla-May, K. Weber and J. Popp, Towards on-site testing of Phytophthora species, *Anal. Methods*, 2015, **7**, 211–217.

51 L. Schwenkbier, S. Pollok, A. Rudloff, S. Sailer, D. Cialla-May, K. Weber and J. Popp, Non-instrumented DNA isolation, amplification and microarray-based hybridization for a rapid on-site detection of devastating Phytophthora kernoviae, *Analyst*, 2015, **140**, 6610–6618.

52 C. Reuter, N. Slesiona, S. Hentschel, O. Aehlig, A. Breitenstein, A. Csáki, T. Henkel and W. Fritzsche, Loop-mediated amplification as promising on-site detection approach for Legionella pneumophila and Legionella spp, *Appl. Microbiol. Biotechnol.*, 2020, **104**, 405–415.

53 S. Sadhu, T. Paul and N. Yadav, Therapeutic engineering of the gut microbiome using synthetic biology and metabolic tools: a comprehensive review with *E. coli* Nissle 1917 as a model case study, *Arch. Microbiol.*, 2025, **207**, 213.